Pressure-induced superconductivity and nontrivial band topology in compressed γ-InSe

Shiqiu Liu,[1,*] Ye Yang,[1,*] Fanghang Yu,[1] Xikai Wen,[1] Zhigang Gui,[1] Kunling Peng,[1] Rui Wang,[2] and Jianjun Ying[1,†]

[1]*Department of Physics, and CAS Key Laboratory of Strongly-coupled Quantum Matter Physics, University of Science and Technology of China, Hefei, Anhui 230026, China*

[2]*Institute for Structure and Function & Department of physics & Center for Quantum Materials and Devices, Chongqing University, Chongqing 400044, China*

(Received 23 January 2022; revised 2 April 2022; accepted 26 May 2022; published 7 June 2022)

We performed high-pressure electrical transport and Raman measurements on a two-dimensional rhombohedral semiconductor γ-InSe. Our results confirm two structural phase transitions at high pressure. More interestingly, a domelike superconducting transition with maximum T_c around 2.3 K is discovered when the compound transforms to the cubic CsCl phase above 40 GPa. Our first-principles calculations indicate that the high-pressure superconducting phase possesses nontrivial topological band structure in the vicinity of the Fermi level. These results show that the physical properties in this material strongly depend on its structure, which provides insights into the interplay between superconductivity and topological physics. Our work suggests promising emergent phenomena in this material and other related III-VI semiconductors under high-pressure conditions.

DOI: 10.1103/PhysRevB.105.214506

I. INTRODUCTION

Since the discovery of graphene [1], two dimensional (2D) semiconductors have attracted tremendous interest since they offer fascinating opportunities in the field of microelectronic and optoelectronic devices due to their novel properties. One of the layered III-VI semiconductors, InSe, has attracted extensive attention recently due to its potential application in the fields of optoelectronics and thermoelectric devices [2–12]. InSe exhibits high photoresponsivity, excellent electrical properties, and nonlinear optical effect [3,7]. However, its physical properties under extreme conditions were not fully explored and more experiments are needed to search for its emergent phenomena.

At ambient conditions, InSe crystallizes in the layered rhombohedral phase [13], built as a stack of 2D layers formed by two honeycomb In-Se sheets which are bound by strong In-In covalent bonds; layers are bound by weak van der Waals forces. InSe crystals can exist in three polytypes denoted as β, γ, and ε phases. γ-InSe is the most studied polytype with ABCABC stacking arrangement as shown in Fig. 1(a). Monolayer and few-layer γ-InSe have been proved [7] to possess high electron mobility in the order of 10^3 cm^2 V^{-1} s^{-1}, and the band gap of γ-InSe is highly tunable in the few-layers regime possibly related to the strong quantum confinement effect [7,14–22]. Since γ-InSe posseses the excellent metal contact and moderate band gap range [23], it is proposed to offer the opportunity for presenting tunable nanodevices [16,24,25]. The InSe flake photodetectors were broad spectra responsive from visible light to near infrared [26]. Ultrahigh photoresponsivity and detectivity were achieved in InSe nanosheet photodetectors [27]. Optimization and tuning of its structure symmetry or/and lattice parameters may enhance the electronic, optoelectronic, and thermoelectric performances, as well as lead to novel physical phenomena. A robust layered indium selenide (InSe) field-effect transistor (FET) delivers a high electron mobility up to 3700 cm^2 V^{-1} s^{-1} at room temperature by depositing an indium (In) doping layer [28]. Besides doping, high pressure is another effective method to provide such tuning of the physical properties of the materials [29]. By applying high pressure, crystal structure can be significantly modified and many interesting physical phenomena emerge, such as superconductivity [29]. Early high-pressure works [30] indicate that γ-InSe can transit to the cubic rocksalt phase and cubic CsCl phase at high pressure [30]. However, the physical properties of the high-pressure phases are still not well studied. In addition, the band structure is strongly related to the crystal structure. It is also interesting to check whether a nontrivial topological band structure emerges in the high-pressure phase. Here, we combined the high-pressure Raman and electrical transport measurements on this layered material γ-InSe. We confirmed two structural phase transitions at high pressure. More interestingly, the domelike superconductivity emerges in the cubic CsCl phase. The maximum T_c is around 2.3 K around 44 GPa; such a domelike T_c behavior is similar to the compressed nonmagnetic topological line-nodal material $CaSb_2$ [31]. The first-principles calculations indicate that the high-pressure superconducting phase possesses a nontrivial topological band structure.

II. METHODS

High quality single crystals with nominal composition InSe were grown by the Bridgman method [32]. We conducted the

*These authors contributed equally to this work.
†yingjj@ustc.edu.cn

 ©2022 American Physical Society

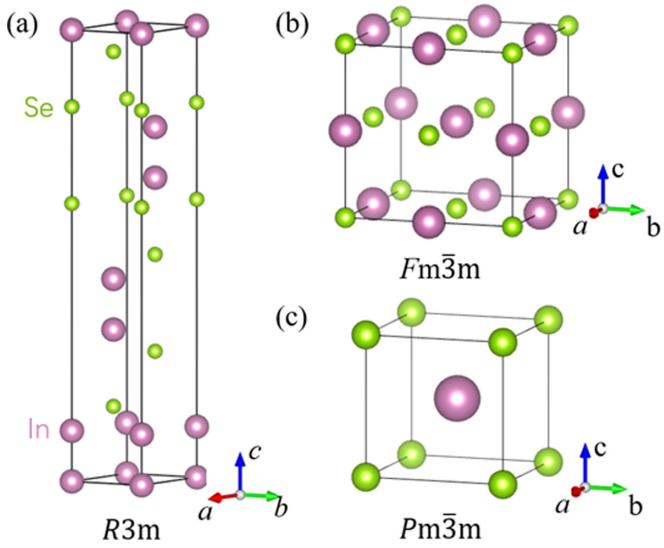

FIG. 1. (a) Representation of structure for γ-InSe at ambient pressure with space group $R3m$. (b), (c) Representations of high-pressure structures with space group $Fm\bar{3}m$ and $Pm\bar{3}m$.

electrical transport measurements on γ-InSe single crystals under pressure by using the miniature diamond anvil cell. Diamond anvils with 300-μm culets and sample chambers of diameter 80 μm were used for the high-pressure electrical transport measurements which could generate the pressure above 50 GPa. c-BN was used as the insulating layer between the electric probes and the rhenium gasket, which is made by compressing the c-BN + epoxy up to 25 GPa. The crystal was cut with the dimensions of $60\times60\times10\,\mu m^3$ and NaCl was used as a pressure-transmitting medium. Resistivity and Hall coefficient were measured using the van der Pauw method in a Quantum Design Physical Properties Measurement System. A diamond anvil with a 300-μm culet was used for the high-pressure Raman measurements with incident laser wavelength of 532 nm. Daphne 7373 oil was loaded as the pressure transmitting medium. Pressure was calibrated by using ruby fluorescence shift at room temperature for both the transport and Raman measurements.

First-principles calculations based on the density functional theory (DFT) [33] are implemented in the Vienna ab initio simulation package (VASP) [34], in which the Perdew-Burke-Ernzerhof (PBE) functional [35] is used to describe the exchange correlation energy. The plane-wave-basis cutoff energy is set to 450 eV for treating the core-valence interactions, and the convergence criterion of structural relaxation is 10^{-7} eV in energy and 10^{-3} eV/Å in force. The Brillouin zone (BZ) is sampled by a $14\times14\times14$ Monkhorst-Pack grid [36]. The Z_2 topological invariant is obtained from the parity eigenvalues at time-reversal invariant momentum (TRIM)points, which are performed by using the IRVSP package [37].

III. RESULTS AND DISCUSSION

InSe single crystals grown by the Bridgman method above at ambient conditions is γ-InSe, as shown in Fig. 1(a), which belongs to space group $R3m$ [13]. Figures 1(b) and 1(c) shows the high-pressure structures of the cubic rocksalt phase (space group Fm-$3m$) and cubic CsCl phase (space group Pm-$3m$), respectively. Previous high-pressure x-ray diffraction (XRD) indicates the layered rhombohedral structure transforms to the rocksalt structure around 10 GPa at room temperature [30]. Above 40 GPa, the rocksalt structure turns to the cubic CsCl structure [30].

In order to search for the new physical phenomena under pressure, we performed high-pressure resistivity measurement with current applied along the ab plane on the rhombohedral γ-InSe single crystal. Figure 2(a) shows the temperature dependence of the resistivity for γ-InSe at various pressures up to 40.6 GPa. Below 8.1 GPa, the resistivity shows an insulating behavior and the resistivity can be gradually suppressed with increasing the pressure. With pressure above 11 GPa, the resistivity slightly increases with increasing the pressure, which is probably due to the structural transition from rhombohedral structure to rocksalt structure. The resistivity starts to decrease above 23.4 GPa and shows metallic behavior with the pressure above 40 GPa as shown in Fig. 2(c). More interestingly, the resistivity shows a sudden drop at low temperature with pressure above 40 GPa. Such sharp decrease of the resistivity is due to the superconducting transition; zero resistivity is reached around 44 GPa and T_c reaches its maximum value of 2.3 K as shown in Fig. 2(d). The superconducting transition temperature T_c can be gradually suppressed by further increasing the pressure. The discovery of superconductivity in InSe adds insight into the physics in III-VI semiconductors under high-pressure conditions. It can be seen that the resistivity at 10 and 300 K which is extracted from the temperature dependence of resistivity curves changes significantly around 10 GPa and around 40 GPa as shown in Fig. 2(b), consistent with the previous research [30] which reports two structural phase transitions at high pressure. This result is also supported by the changes in Hall coefficient and mobility at 10 K around 10 and 40 GPa in Fig. 2(b). The Hall resistivity measured at 10 K under various pressures were shown in Supplemental Material Fig. S1 [38]. The negative Hall coefficient indicates the electron is the primary carrier despite the different structures at high pressure. More interestingly, the Hall coefficient is nearly invariant in the rocksalt phase and starts to decrease when the sample evolves to the CsCl phase, indicating the enhancement of the carrier density at high pressure which may be quite crucial to the superconductivity.

The observed superconductivity in InSe was further supported by the evolution of the resistivity-temperature curve with the magnetic fields applied along the c axis as shown in Fig. 3. The sudden drop of the resistivity curves gradually shift towards the lower temperature with increasing the magnetic field. It can be seen that 0.13 T is sufficient to suppress superconductivity below 2 K at 40.6 GPa. We can estimate the upper critical field (H_{c2}) from these resistivity curves. The H_{c2} shows a linear dependence with respect to the T_c as shown in Fig. 3. Within the weak-coupling BCS theory, the upper critical field at $T = 0$ K can be determined by the Werthamer-Helfand-Hohenberg (WHH) equation [39] $H_{c2}(0) = 0.693[-(dH_{c2}/dT)]_{T_c}T_c$. We can deduce that $H_{c2}(0)\sim0.66$ T.

Raman experiments on III-VI layered materials under high pressure have been used as a tool to investigate the struc-

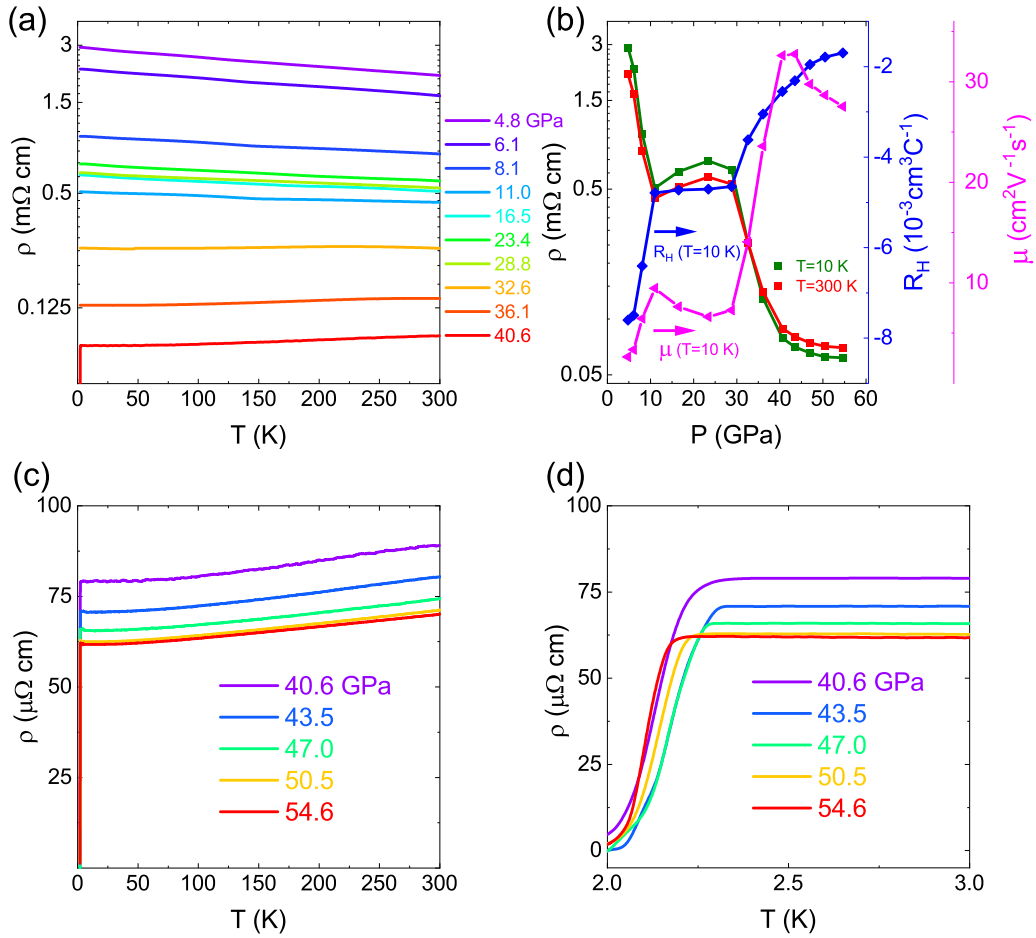

FIG. 2. (a) Temperature dependence of the resistivity for γ-InSe up to 40.6 GPa. (b) Pressure dependence of the resistivity (at 10 and 300 K), Hall coefficient (at 10 K), and mobility (at 10 K) for γ-InSe. Panels (c) and (d) show the emergence of superconductivity above 40 GPa and the maximum T_c is about 2.3 K around 44 GPa.

ture stability [40–42]. In order to further study the structural evolution and phase transition of InSe, we have measured

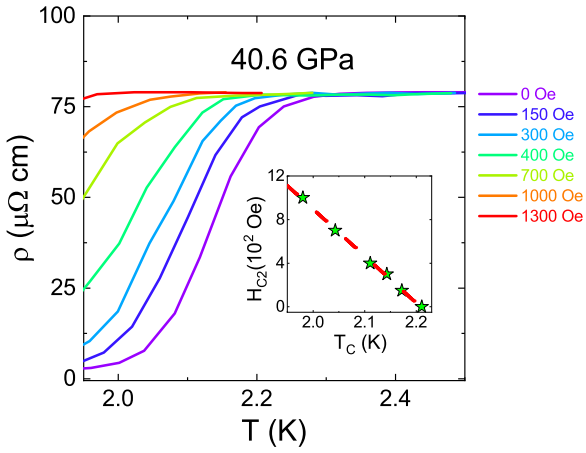

FIG. 3. Temperature dependence of the resistivity for γ-InSe with the pressure of 40.6 GPa under various magnetic fields. Inset: Upper critical field H_{c2} for pressure at 40.6 GPa. T_c was determined from the 90% resistivity transition.

the Raman spectroscopy at room temperature as shown in Fig. 4. Figure 4(a) shows the Raman spectra of InSe at various pressures up to 10 GPa. Three Raman peaks located at 114, 175, and 224 cm^{-1} can be observed at ambient pressure in our experiments, which correspond to A^1_{1g}, E^1_{2g}, A^2_{1g} modes, respectively [21,43–45]. As the pressure increases, all the three Raman modes linearly shift to higher wave numbers as shown in Fig. 4(b). When the pressure is above 10 GPa, all the peaks disappear, which indicates that the sample transformation to the rocksalt phase is complete. Our Raman results are consistent with the structural phase transition proposed from the previous research [30].

By combining the high-pressure resistivity and Raman results, we can map out the phase diagram as shown in Fig. 5. We can clearly see that the resistivity suddenly changes across the two structural phase transitions around 10 and 40 GPa. The different colors in Fig. 5 represent the different phases, and the phase boundaries determined from our work are consistent with previous XRD studies [30].

Using first-principles calculations based on the density functional theory (DFT), we investigate the evolution of electronic structures of InSe with the increase of pressure. The calculated results of InSe with CsCl structure under 50 GPa

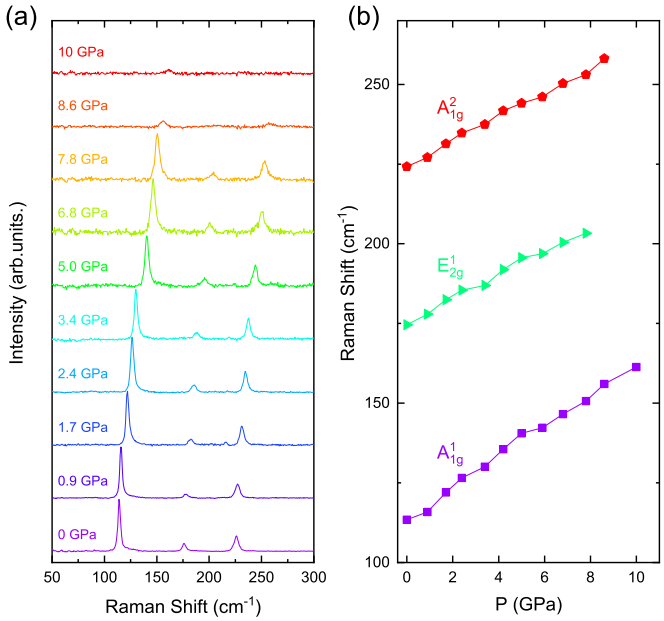

FIG. 4. (a) Raman spectra of γ-InSe at various pressures up to 10 GPa at room temperature. The Raman modes disappears above 10 GPa due to the structural phase transition. (b) Pressure dependence of the three Raman modes at room temperature.

are present in Fig. 6. As shown in Figs. 6(a) and 6(b), the band structures of InSe exhibit the typical metallic behavior with electronlike Fermi pockets under 50 GPa, consistent with the experimental observation. The projected DOS indicates that In-s, In-p, and Se-p states significantly contribute to bands near the Fermi level [see Fig. 6(c)]. We further analyze the topological properties of InSe under 50 GPa. In the absence of spin-orbital coupling (SOC), it is found that band crossings occur along the X-M and M-Γ paths in the vicinity of the Fermi level, respectively [see Fig. 6(a)]. These two intersecting bands along the X-M path (or the M-Γ path) belong to different irreducible representations (IRs) Γ_1 and Γ_2 of the mirror reflection symmetry, forming the nodal ring with respect to the band inverted point M. Since the crystal structure of InSe under 50 GPa hosts the inversion (I) and time-reversal (T) symmetries, this nodal ring is protected by the combination of IT symmetry. In addition, the mirror symmetry M_i ($i = x, y, z$) guarantees that the nodal ring is present on the reflection-invariant plane. Considering the fourfold rotational symmetry, there are 12 Dirac nodal rings symmetrically distributed in the BZ of InSe. As shown in Fig. 6(b), the presence of SOC can gap the nodal rings due to the spin-rotation symmetry breaking. The calculated band gaps along the X-M and M-Γ paths are 136 and 66 meV, respectively. Due to the existence of continuous band gaps between bands near the Fermi level, we can calculate the parity eigenvalues at the time-reversal invariant momentum (TRIM) points to reveal band topology. As illustrated in Fig. 6(d), considering band 7 as the occupied band, the system exhibits a strong topological invariant $Z_2 = (1;000)$, while band 9 and band 5 are topologically trivial. Therefore, the gapped nodal rings induced by SOC are topologically nontrivial.

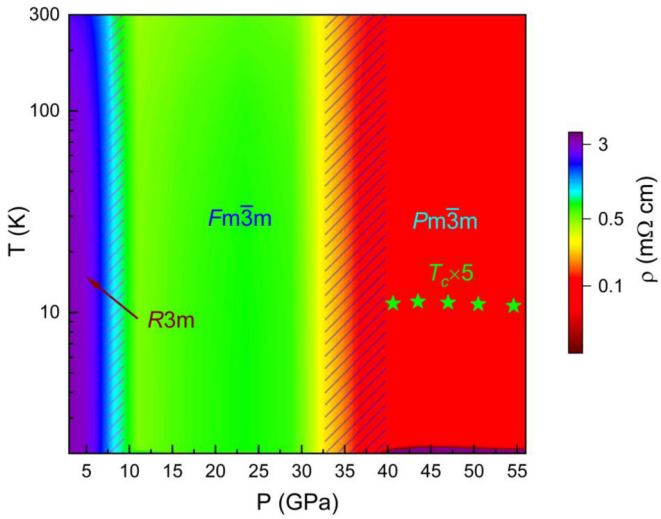

FIG. 5. The phase diagram of γ-InSe at high pressure. Superconductivity emerges above 40 GPa. The color represents the magnitude of the resistivity measured under various pressures and temperatures.

From our first-principles calculations as presented in Supplemental Material Figs. S2 and S3 [38], we found that the insulating ambient-pressure phase would transfer to the metallic rocksalt phase, consistent with our transport measurements. More interestingly, our work demonstrates that InSe becomes the superconductor when the structure turns to CsCl type at high pressure. Pressure-induced superconductivity is also observed in another layered III-VI semiconductor, GaSe, in which superconductivity up to 5 K is discovered above 25 GPa [46]. However, in contrast to our case, the structure of the superconducting GaSe phase is the rocksalt type rather than the CsCl type [47]. More strikingly, the superconducting phase possesses a nontrivial band structure, which makes this material a prototype to study the interplay of topology and superconductivity.

IV. CONCLUSION

In summary, we investigate in detail the pressure effect on the layered rhombohedral semiconductor γ-InSe. Our high-pressure transport and Raman experiments confirm two structural phase transitions at high pressure, consistent with previous results [30]. Superconductivity was observed in the CsCl-type phase. Our first-principles calculations reveal the nontrivial topological band structure of the superconducting CsCl-type phase, which provides an interesting playground to study the interplay of superconductivity and topology in this material and other related III-VI semiconductors under high-pressure conditions.

ACKNOWLEDGMENTS

This work was supported by the National Key Research and Development Program of the Ministry of Science and Technology of China (Grant No. 2019YFA0704900), the Collaborative Innovation Program of Hefei Science Center, CAS (Grant No. 2020HSC-CIP014), and the Fundamental Research Funds for the Central Universities (Grant No. WK3510000011).

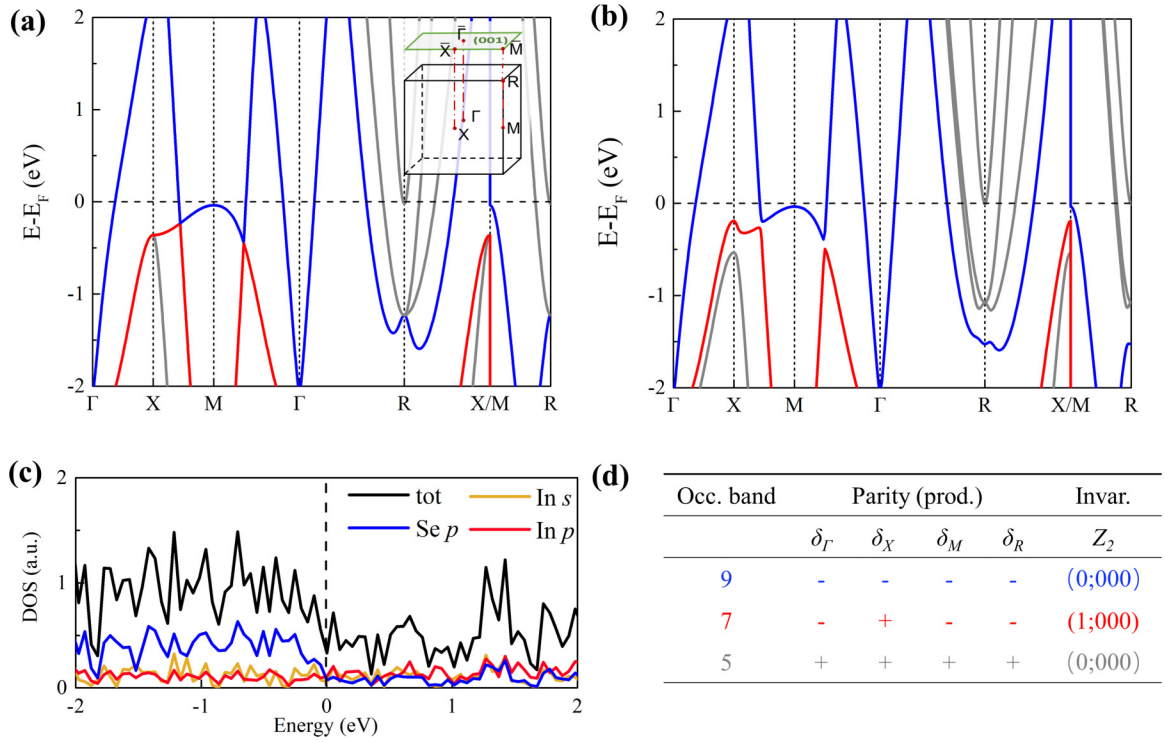

Occ. band	Parity (prod.)				Invar.
	δ_Γ	δ_X	δ_M	δ_R	Z_2
9	-	-	-	-	(0;000)
7	-	+	-	-	(1;000)
5	+	+	+	+	(0;000)

FIG. 6. The electronic structure and topological classification for the cubic CsCl-structure InSe under 50 GPa. (a),(b) The calculated band structures of InSe without SOC and with SOC. Inset: The cubic bulk Brillouin zone (BZ) and projected [001] surface BZ with labeled high symmetry points. (c) Projected density of states (DOS) of InSe without SOC. (d) The parity at TRIMs and the Z_2 invariant for bands close to the Fermi level in InSe. δ_X denotes the parity eigenvalues at the time-invariant "X" point.

[1] K. S. Novoselov, A. K. Geim, S. V. Morozov, D. Jiang, Y. Zhang, S. V. Dubonos, I. V. Grigorieva, and A. A. Firsov, Science **306**, 666 (2004).

[2] N. T. Hung, A. R. T. Nugraha, and R. Saito, Appl. Phys. Lett. **111**, 092107 (2017).

[3] Z. S. Chen, C. Giorgetti, J. Sjakste, R. Cabouat, V. Veniard, Z. L. Zhang, A. Taleb-Ibrahimi, E. Papalazarou, M. Marsi, A. Shukla, J. Peretti, and L. Perfetti, Phys. Rev. B **97**, 241201(R) (2018).

[4] N. T. Hung, A. R. T. Nugraha, T. Yang, Z. D. Zhang, and R. Saito, J. Appl. Phys. **125**, 082502 (2019).

[5] Q. Y. Hao, J. D. Liu, G. Wang, J. W. Chen, H. B. Gan, J. Q. Zhu, Y. X. Ke, Y. Chai, J. H. Lin, and W. J. Zhang, ACS Nano **14**, 11373 (2020).

[6] Y. Y. Lu, C. R. Guo, H. L. Yeh, H. W. Chen, C. C. Kuo, J. H. Hsu, J. Jhou, Y. T. Huang, S. H. Hsieh, C. H. Chen, C. H. Ho, R. Sankar, and F. C. Chou, ACS Appl. Nano Mater. **3**, 11769 (2020).

[7] D. A. Bandurin, A. V. Tyurnina, G. L. Yu, A. Mishchenko, V. Zolyomi, S. V. Morozov, R. K. Kumar, R. V. Gorbachev, Z. R. Kudrynskyi, S. Pezzini, Z. D. Kovalyuk, U. Zeitler, K. S. Novoselov, A. Patane, L. Eaves, I. V. Grigorieva, V. I. Fal'ko, A. K. Geim, and Y. Cao, Nat. Nanotechnol. **12**, 223 (2017).

[8] C. X. Xia, J. Du, X. W. Huang, W. B. Xiao, W. Q. Xiong, T. X. Wang, Z. M. Wei, Y. Jia, J. J. Shi, and J. B. Li, Phys. Rev. B **97**, 115416 (2018).

[9] M. J. Dai, H. Y. Chen, F. K. Wang, Y. X. Hu, S. Wei, J. Zhang, Z. G. Wang, T. Y. Zhai, and P. A. Hu, ACS Nano **13**, 7291 (2019).

[10] K. Jin, T. S. Li, H. B. Cai, M. L. Li, N. Pan, and X. P. Wang, Opt. Commun. **436**, 47 (2019).

[11] Y. J. Yang, J. Jeon, J. H. Park, M. S. Jeong, B. H. Lee, E. Hwang, and S. Lee, ACS Nano **13**, 8804 (2019).

[12] D. S. Ziyad and B. R. Fikret, Mol. Cryst. Liq. Cryst. **717**, 47 (2021).

[13] A. Likforman, D. Carre, J. Etienne, and B. Bachet, Acta Crystallogr. Sect. B: Struct. Sci. **31**, 1252 (1975).

[14] S. Yang and D. F. Kelley, J. Phys. Chem. B **109**, 12701 (2005).

[15] S. Yang and D. F. Kelley, J. Phys. Chem. B **110**, 13430 (2006).

[16] G. W. Mudd, S. A. Svatek, T. Ren, A. Patanè, O. Makarovsky, L. Eaves, P. H. Beton, Z. D. Kovalyuk, G. V. Lashkarev, Z. R. Kudrynskyi, and A. I. Dmitriev, Adv. Mater. **25**, 5714 (2013).

[17] G. W. Mudd, A. Patanè, Z. R. Kudrynskyi, M. W. Fay, O. Makarovsky, L. Eaves, Z. D. Kovalyuk, V. Zólyomi, and V. Falko, Appl. Phys. Lett. **105**, 221909 (2014).

[18] J. F. Sánchez-Royo, G. Muñoz-Matutano, M. Brotons-Gisbert, J. P. Martínez-Pastor, A. Segura, A. Cantarero, R. Mata, J. Canet-Ferrer, G. Tobias, E. Canadell, J. Marqués-Hueso, and B. D. Gerardot, Nano Res. **7**, 1556 (2014).

[19] M. Brotons-Gisbert, D. Andres-Penares, J. Suh, F. Hidalgo, R. Abargues, P. J. Rodríguez-Cantó, A. Segura, A. Cros, G. Tobias, E. Canadell, P. Ordejón, J. Wu, J. P. Martínez-Pastor, and J. F. Sánchez-Royo, Nano Lett. **16**, 3221 (2016).

[20] G. W. Mudd, M. R. Molas, X. Chen, V. Zólyomi, K. Nogajewski, Z. R. Kudrynskyi, Z. D. Kovalyuk, G. Yusa, O. Makarovsky, L. Eaves, M. Potemski, V. I. Fal'ko, and A. Patanè, Sci. Rep. **6**, 39619 (2016).

[21] T. Zheng, Z. T. Wu, H. Y. Nan, Y. F. Yu, A. Zafar, Z. Z. Yan, J. P. Lu, and Z. H. Ni, RSC Adv. **7**, 54964 (2017).

[22] C. Song, F. Fan, N. Xuan, S. Huang, G. Zhang, C. Wang, Z. Sun, H. Wu, and H. Yan, ACS Appl. Mater. Interfaces **10**, 3994 (2018).
[23] K. Xu, L. Yin, Y. Huang, T. A. Shifa, J. Chu, F. Wang, R. Cheng, Z. Wang, and J. He, Nanoscale **8**, 16802 (2016).
[24] S. Lei, L. Ge, S. Najmaei, A. George, R. Kappera, J. Lou, M. Chhowalla, H. Yamaguchi, G. Gupta, R. Vajtai, A. D. Mohite, and P. M. Ajayan, ACS Nano **8**, 1263 (2014).
[25] G. W. Mudd, S. A. Svatek, L. Hague, O. Makarovsky, Z. R. Kudrynskyi, C. J. Mellor, P. H. Beton, L. Eaves, K. S. Novoselov, Z. D. Kovalyuk, E. E. Vdovin, A. J. Marsden, N. R. Wilson, and A. Patanè, Adv. Mater. **27**, 3760 (2015).
[26] S. R. Tamalampudi, Y.-Y. Lu, K. U R., R. Sankar, C.-D. Liao, M. B K., C.-H. Cheng, F. C. Chou, and Y.-T. Chen, Nano Lett. **14**, 2800 (2014).
[27] W. Feng, J.-B. Wu, X. Li, W. Zheng, X. Zhou, K. Xiao, W. Cao, B. Yang, J.-C. Idrobo, L. Basile, W. Tian, P. Tan, and P. Hu, J. Mater. Chem. C **3**, 7022 (2015).
[28] M. J. Li, C. Y. Lin, S. H. Yang, Y. M. Chang, J. K. Chang, F. S. Yang, C. R. Zhong, W. B. Jian, C. H. Lien, C. H. Ho, H. J. Liu, R. Huang, W. W. Li, Y. F. Lin, and J. H. Chu, Adv. Mater. **30**, 1803690 (2018).
[29] H.-K. Mao, X.-J. Chen, Y. Ding, B. Li, and L. Wang, Rev. Mod. Phys. **90**, 015007 (2018).
[30] A. Segura, Crystals **8**, 206 (2018).
[31] S. Kitagawa, K. Ishida, A. Ikeda, M. Kawaguchi, S. Yonezawa, and Y. Maeno, Phys. Rev. B **104**, L060504 (2021).
[32] A. Chevy, A. Kuhn, and M. S. Martin, J. Cryst. Growth **38**, 118 (1977).
[33] W. Kohn and L. J. Sham, Phys. Rev. **140**, A1133 (1965).
[34] G. Kresse and J. Furthmüller, Phys. Rev. B **54**, 11169 (1996).
[35] J. P. Perdew, K. Burke, and M. Ernzerhof, Phys. Rev. Lett. **77**, 3865 (1996).
[36] H. J. Monkhorst and J. D. Pack, Phys. Rev. B **13**, 5188 (1976).
[37] J. Gao, Q. Wu, C. Persson, and Z. Wang, Comput. Phys. Commun. **261**, 107760 (2021).
[38] See Supplemental Material at http://link.aps.org/supplemental/10.1103/PhysRevB.105.214506 for further details on the experimental measurements and first-principles calculations.
[39] N. R. Werthamer, E. Helfand, and P. C. Hohenberg, Phys. Rev. **147**, 295 (1966).
[40] K. Allahverdi, S. Babaev, S. Ellialtioglu, and A. Ismailov, Solid State Commun. **87**, 675 (1993).
[41] A. Polian, J. C. Chervin, and J. M. Besson, Phys. Rev. B **22**, 3049 (1980).
[42] M. Gauthier, A. Polian, J. M. Besson, and A. Chevy, Phys. Rev. B **40**, 3837 (1989).
[43] N. M. Gasanly, B. M. Yavadov, V. I. Tagirov, and E. A. Vinogradov, Phys. Status Solidi B **89**, K43 (1978).
[44] C. Ulrich, M. A. Mroginski, A. R. Goni, A. Cantarero, U. Schwarz, V. Munoz, and K. Syassen, Phys. Status Solidi B **198**, 121 (1996).
[45] M. Wu, Q. Xie, Y. Wu, J. Zheng, W. Wang, L. He, X. Wu, and B. Lv, AIP Advances **9**, 025013 (2019).
[46] K. J. Dunn and F. P. Bundy, Appl. Phys. Lett. **36**, 709 (1980).
[47] U. Schwarz, D. Olguin, A. Cantarero, M. Hanfland, and K. Syassen, Phys. Status solidi B **244**, 244 (2007).